Nonthermal and reversible control of neuronal signaling and behavior by midinfrared stimulation

Xi Liu[a,b,1] , Zhi Qiao[c,d,1] , Yuming Chai[e,f,1] , Zhi Zhu[g,1] , Kaijie Wu[c] , Wenliang Ji[h] , Daguang Li[e,f] , Yujie Xiao[a,b] , Lanqun Mao[h], Chao Chang[c,d,2] , Quan Wen[e,f,2] , Bo Song[g,2], and Yousheng Shu[i,2]

aState Key Laboratory of Cognitive Neuroscience and Learning, Beijing Normal University, Beijing 100875, China; bIDG/McGovern Institute for Brain Research, Beijing Normal University, Beijing 100875, China; cKey Laboratory for Physical Electronics and Devices of the Ministry of Education, School of Electronic and Information Engineering, Xi'an Jiaotong University, Xi'an, Shaanxi 710049, China; dInnovation Laboratory of Terahertz Biophysics, National Innovation Institute of Defense Technology, Beijing 100071, China; eHefei National Laboratory for Physical Sciences at the Microscale Center for Integrative Imaging, School of Life Sciences, University of Science and Technology of China, Hefei 230027, China; fKey Laboratory of Brain Function and Disease, Chinese Academy of Sciences, Hefei 230027, China; gSchool of Optical-Electrical Computer Engineering, University of Shanghai for Science and Technology, Shanghai 200093, China; hBeijing National Laboratory for Molecular Sciences, Key Laboratory of Analytical Chemistry for Living Biosystems, Institute of Chemistry, Chinese Academy of Sciences, Beijing 100190, China; and iDepartment of Neurology, Huashan Hospital, State Key Laboratory of Medical Neurobiology, Institute for Translational Brain Research, MOE Frontiers Center for Brain Science, Fudan University, Shanghai 200032, China

Various neuromodulation approaches have been employed to alter neuronal spiking activity and thus regulate brain functions and alleviate neurological disorders. Infrared neural stimulation (INS) could be a potential approach for neuromodulation because it requires no tissue contact and possesses a high spatial resolution. However, the risk of overheating and an unclear mechanism hamper its application. Here we show that midinfrared stimulation (MIRS) with a specific wavelength exerts nonthermal, long-distance, and reversible modulatory effects on ion channel activity, neuronal signaling, and sensorimotor behavior. Patch-clamp recording from mouse neocortical pyramidal cells revealed that MIRS readily provides gain control over spiking activities, inhibiting spiking responses to weak inputs but enhancing those to strong inputs. MIRS also shortens action potential (AP) waveforms by accelerating its repolarization, through an increase in voltage-gated K^+ (but not Na^+) currents. Molecular dynamics simulations further revealed that MIRS-induced resonance vibration of $-C=O$ bonds at the K^+ channel ion selectivity filter contributes to the K^+ current increase. Importantly, these effects are readily reversible and independent of temperature increase. At the behavioral level in larval zebrafish, MIRS modulates startle responses by sharply increasing the slope of the sensorimotor input–output curve. Therefore, MIRS represents a promising neuromodulation approach suitable for clinical application.

action potential | excitability | infrared light | neuromodulation | potassium channel

Many forms of neuromodulation have been used for the regulation of brain functions and the treatment of brain disorders. Some physical approaches, such as electrical, magnetic, and optical (electromagnetic; EM) stimulation could be employed to manipulate neural spiking activity and achieve neuromodulation. Among them, deep-brain electrical stimulation has become a gold standard treatment for advanced Parkinson's disease; transcranial magnetic stimulation also generates electrical current in selected brain regions and has been used for mood regulation. In contrast, optical neural stimulation has not been used clinically, largely due to the risk of tissue damage by overheating and unclear mechanisms. Although optogenetic manipulation and stimulation avoid these problems and show cell specificity, the requirement of expression of exogenous genes hinders its use in humans (1).

Optical infrared neural stimulation (INS) is emerging as an area of interest for neuromodulation and potential clinical application. INS utilizes brief light pulses to activate excitable cells or tissues in the illumination spot. Previous studies showed that INS could activate peripheral nerves (2), peripheral sensory systems (3, 4), and cardiac tissue (5). In the central nervous system (CNS), initial studies found that INS could evoke neural responses in rat thalamocortical slices in vitro (6) and regulate spiking activity in rodent somatosensory cortex (7) and nonhuman primate visual cortex in vivo (8). Because of its high spatial precision, focal INS has been recently applied to map brain connectomes (9). The underlying mechanism of INS, however, remains poorly understood. The predominant view is the transduction of EM energy to thermal heat (10, 11) will excite the cell, possibly due to heat-induced transmembrane capacitive charge (12), changes in ion channel activity (13), or cell damage (14). Since previous studies tended to choose infrared wavelengths with high water absorption for efficient heat generation, it remains unclear whether INS exerts nonthermal effects on ion channel and neuronal spiking activity.

While most studies on infrared stimulation have been conducted at near-infrared wavelengths, whether midinfrared wavelengths can regulate neural function is unknown. Because the frequency of midinfrared light falls into the frequency range of chemical bond vibration (15–17), nonlinear resonances may occur within biomolecules (18–20), leading to dramatic changes in their

Significance

Infrared neural stimulation (INS) is an emerging technology for neuromodulation and holds promise for clinical application. While most INS studies have been conducted at near-infrared wavelengths, whether midinfrared light with frequencies matching the chemical bond vibration of biomolecules can influence neuronal function remains unknown. We found that midinfrared light with low water absorption provides nonthermal and reversible modulation of neuronal spiking activity and sensorimotor behavior. Nonlinear resonance between light and chemical bond vibration at the selectivity sieve of the K^+ channel directly enhances ion conductivity and thus regulates AP waveform and spiking activity. Together, our results reveal nonthermal effects of MIRS on functional biomolecules, neuronal signaling, and behavior state. Therefore, MIRS could serve as a form of physical neuromodulation.

conformation and function (21) and thus producing nonthermal effects on biological systems. Ion channel proteins distributed on cell membranes could be potential molecular targets for midinfrared light. Among them, voltage-gated Na$^+$ and K$^+$ channels play critical roles in regulating the initiation and propagation of the action potential (AP), an all-or-none digital signal of neurons (22, 23). They also control the voltage waveform of the AP and thus the size of the postsynaptic response, ensuring analog-mode communication between neurons (24–27). It is of interest to know whether midinfrared stimulation (MIRS) can cause conformational change in these channel proteins and consequently regulate neuronal signaling. Previous studies revealed a low absorption of light by water in the midinfrared region from 3.5 to 5.7 μm (28), which could be a potential wavelength range for neuromodulation. Therefore, in this study, we explored whether MIRS with a specific wavelength in this range could exert nonthermal modulatory effects on channel activity, neuronal signaling, and behavior.

Results

MIRS Exerts Gain Modulation of Neuronal Spiking Activity. Infrared light may produce thermal heat, particularly at those wavelengths with high absorption in water; we thus chose a midinfrared wavelength (5.6 μm) with low attenuation of light in artificial cerebrospinal fluid (ACSF; *SI Appendix*, Fig. S1) to avoid excessive heat (28). The power density in air at the laser fiber tip was ~110 μW/μm^2. In the slice recording chamber perfused with ACSF (0.9 mL/min), carbon fiber electrodes (naked tip diameter: 7 μm; length: 20 μm) with a holding potential of 780 mV were employed to measure local temperature changes using the Arrhenius equation (29) (Fig. 1 *A* and *B* and *SI Appendix, Methods*). When MIRS was applied, the temperature 70 μm away from the optical fiber tip (i.e., light source) increased by ~6 °C, from 24.9 ± 0.2 to 30.4 ± 0.4 °C (mean ± SEM, n = 12; Fig. 1C). The temperature increase took

2 to 4 s to reach a plateau (Fig. 1B). Negligible temperature change was detected if the distance along the fiber axis was greater than 200 μm (ΔT: 0.52 ± 0.79 °C; 300 μm: −0.21 ± 0.73 °C, n = 4; Fig. 1D). In the following experiments, the duration of MIRS varied from 10 to 200 s covering the whole periods of testing for MIRS effects.

To examine the effect of MIRS on neuronal excitability, we performed whole-cell current-clamp recording from layer-5 pyramidal cells (PCs) in acute slices of mouse prefrontal cortex and compared the input–output (*I–F*) curves before and during MIRS (Fig. 1 *E–G*). We recorded cells 300 μm away from the laser fiber tip to exclude effects induced by the temperature increase. We found no significant change in the resting membrane potential (V_m) during MIRS; however, the input resistance (R_{in}) was reduced from 194 ± 17 to 169 ± 14 MΩ (n = 9 cells, $t_8 = -6.91$, $P = 0.1 \times 10^{-3}$, paired Student's *t* test), and the membrane time constant τ also decreased substantially (Fig. 1H). Interestingly, MIRS significantly reduced neuronal responsiveness to small current pulses less than 200 pA but enhanced that to large current injections (>400 pA; Fig. 1 *F* and *G*). The threshold current (rheobase) for AP generation showed a substantial increase (Fig. 1H). The slope of the *I–F* curve increased significantly from 0.037 ± 0.002 to 0.052 ± 0.001 Hz/pA (n = 9, $t_8 = -8.51$, $P = 0.3 \times 10^{-4}$, paired Student's *t* test), indicating a gain control of neuronal responses by MIRS. Importantly, during MIRS the recorded neuron continued to produce high-frequency APs in response to strong current pulses, which could cause inactivation of Na$^+$ channels and thus the absence of spikes (i.e., depolarization block) in control conditions (Fig. 1 *F* and *G*). Similar findings were obtained when we recorded the cells at a physiological temperature of 36 °C (*SI Appendix*, Fig. S2). Considering that the basal dendrites and axon collaterals may extend to a region near the fiber tip, we made a knife cut from pia to
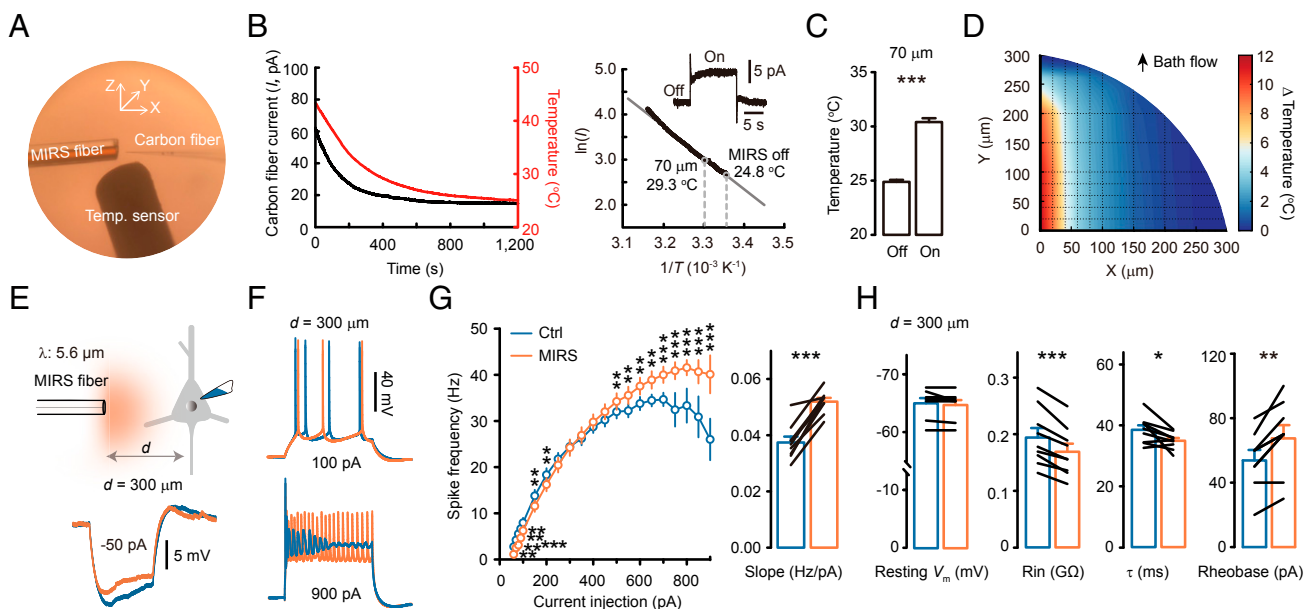

Fig. 1. Nonthermal effects of MIRS on neuronal excitability. (*A*) Configuration for temperature measurement using a carbon fiber (diameter: 7 μm; naked length: 20 μm). The cladding diameter of the MIRS fiber is 170 μm. (*B, Left*) Change of the measured currents as the bath cools down from ~45 to 25 °C. (*B, Right*) Arrhenius plot of the carbon fiber current (*I*, pA) versus the temperature (*T*, absolute temperature). (*B, Inset*) An example current trace of the carbon fiber induced by MIRS at 70 μm away. (*C*) Measured temperature before and during MIRS. (*D*) A two-dimensional heatmap of temperature change. Note the direction of the bath flow. (*E, Top*) Schematic illustration of MIRS and whole-cell recording from a PC in a prefrontal cortex slice. (*E, Bottom*) Example V_m responses to negative current pulses (500 ms in duration). Blue, control (Ctrl); orange, MIRS. (*F*) Representative spiking responses to positive current pulses. Note the decrease and increase in AP frequency with small and large current pulses, respectively. (*G*) Comparison of *I–F* curves (*Left*) and slopes (*Right*) before and during MIRS at 300 μm away from the cell. (*H*) Group data showing changes in resting V_m, R_{in}, membrane time constant τ, and rheobase current upon MIRS at 300 μm. *$P < 0.05$, **$P < 0.01$, and ***$P < 0.001$. Paired Student's *t* test. Error bars represent SEM.

white matter and recorded PCs near the cut (<80 μm; *SI Appendix*, Fig. S3*A*). MIRS delivered 300 μm away from the cut side of PCs showed similar effects to those without a cut (*SI Appendix*, Fig. S3). Together, these results reveal a nonthermal effect of MIRS on passive membrane property, neuronal excitability, and responsiveness.

Stronger effects were observed when MIRS was applied ~70 μm away from the cell (*SI Appendix*, Fig. S4 *A–C*). MIRS caused a slight but significant depolarization in the resting V_m. Dramatic reductions in the input resistance and the membrane time constant were detected during MIRS. The rheobase increased significantly from 51.4 ± 7.4 to 72.9 ± 9.7 pA ($n = 7$, $t_6 = -8.22$, $P = 0.2 \times 10^{-3}$, paired Student's *t* test). Similarly, neuronal responsiveness to weak and strong current pulses was reduced and enhanced, respectively. Therefore, with MIRS, the slope of the *I–F* curve increased from 0.038 ± 0.003 to 0.064 ± 0.005 Hz/pA ($n = 7$, $t_6 = -7.77$, $P = 0.2 \times 10^{-3}$, paired Student's *t* test). In agreement with these results, MIRS inhibited the repetitive low-frequency firing induced by a small constant-current injection but enhanced the high-frequency firing evoked by a larger direct current (*SI Appendix*, Fig. S4 *D* and *E*). These changes in firing frequency were reversible and reproducible. Since the recorded cell was closer to the light source, these stronger effects may result from increases in both temperature and MIRS power density.

MIRS Alters AP Waveforms. Close examination of the APs recorded at 70 μm revealed a dramatic waveform change (Fig. 2*A*) and the change was readily reversible (*SI Appendix*, Fig. S4 *E* and *F*). The AP peak amplitude showed a slight but significant decrease during MIRS. The half-width and the voltage integral were dramatically reduced (Fig. 2*B*), mainly attributable to an increase in the repolarizing slope (maximum slope: −60.6 ± 1.5 vs. −90.8 ± 2.7 V/s, $t_6 = 9.38$, $P = 0.1 \times 10^{-4}$, paired Student's *t* test). In addition, MIRS increased the amplitude of the afterhyperpolarization from 2.63 ± 0.64 to 6.40 ± 0.82 mV ($n = 7$, $t_6 = -3.82$, $P = 0.009$, paired Student's *t* test). The voltage threshold, however, showed no significant change during MIRS (Fig. 2*B*). We next compared the effects of MIRS with those induced by a 6 °C temperature increase (Fig. 2*C*). The reductions in AP half-width and voltage integral during MIRS were significantly greater than those induced solely

by the temperature increase (Fig. 2*C*). The AP peak amplitude, however, showed similar reduction (to 88.2 ± 1.7% vs. 89.8 ± 2.3%, $Z = -1.04$, $P = 0.34$, Wilcoxon rank-sum test; Fig. 2*C*). These results suggest the existence of nonthermal effects of MIRS on AP waveforms.

In order to investigate the nonthermal effect, we applied MIRS 300 μm away from the cell. Surprisingly, we found similar effects (Fig. 2 *D* and *E*), although the modulatory effect was relatively smaller. MIRS also slightly decreased the AP peak amplitude by ~5%. The AP half-width and voltage integral were dramatically reduced from 1.27 ± 0.08 to 1.0 ± 0.06 ms ($t_8 = 26.9$, $P = 0.4 \times 10^{-8}$) and from 131.7 ± 9.4 to 97.8 ± 5.7 mV·ms ($t_8 = 22.9$, $P = 0.1 \times 10^{-7}$, paired Student's *t* test), mainly due to acceleration of the repolarizing phase (maximum slope: −63.3 ± 4.2 to −77.1 ± 7.1 V/s, $t_8 = 8.65$, $P = 0.2 \times 10^{-4}$, paired Student's *t* test; Fig. 2 *D* and *E*). Together, these experiments demonstrate that MIRS can regulate neuronal signaling, independent of temperature change.

Since the MIRS fiber had a diameter of only 9 μm (much smaller than the distance *d* from the light source to the recorded neuron) and a divergence angle of ~22.5° (*SI Appendix*, Fig. S5), it is physically better considered as a point light source. Thus, we speculated that the distance-dependent reduction of light intensity and then the nonthermal effects of MIRS should follow a relation proportional to $1/d^2$. We used a cable model to simulate the cylinder-like PC that was illuminated by a point light source (Fig. 3 *A* and *B* and *SI Appendix, Methods*). Surprisingly, the normalized AP half-width and voltage integral followed the relation proportional to $1/d$, instead of $1/d^2$. These results indicate that the influence of MIRS decays slowly as *d* increases (i.e., long-distance effect; $n = 19$ cells; Fig. 3*C* and *SI Appendix*, Fig. S6). Note that if a light attenuation coefficient μ in solution (Eq. 3 in *SI Appendix, Methods*) greater than 0.002 μm^{-1} was introduced, the function could not fit the experimental data. Indeed, the measured μ was clearly smaller than this value in ACSF (*SI Appendix*, Fig. S1). These findings indicate a low solution-induced light attenuation at a wavelength of 5.6 μm. Interestingly, the effect of MIRS on AP amplitude decreased sharply within the initial 200 μm and the normalized amplitude correlated well with the temperature increase ($n = 20$; Fig. 3*D* and *SI Appendix*, Fig. S6), indicating that AP amplitude is sensitive to
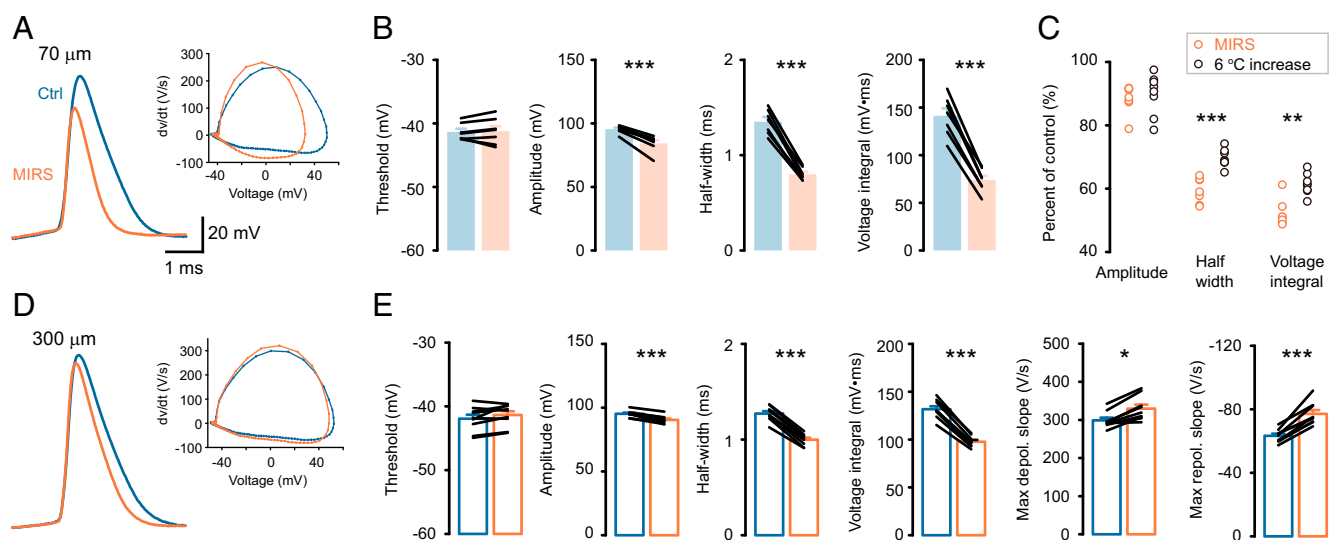
Fig. 2. MIRS causes changes in AP waveforms. (*A–C*) MIRS at 70 μm away from the recorded cell. (*D* and *E*) MIRS at 300 μm away. (*A*) Representative AP waveforms (*Left*) and their phase plots (*Right*) before and during MIRS. (*B*) Comparison of AP parameters before and during MIRS. (*C*) Comparison of the changes in peak amplitude, half-width, and voltage integral of APs with MIRS and by an increase in temperature (6 °C, gray). (*D*) Representative AP waveforms and their phase plots before and during MIRS at 300 μm away. (*E*) Comparison of AP parameters. *$P < 0.05$, **$P < 0.01$, and ***$P < 0.001$. Paired Student's *t* test (*B* and *E*) and independent Wilcoxon rank-sum test (*C*). Error bars represent SEM.

Liu et al.
Nonthermal and reversible control of neuronal signaling and behavior by midinfrared stimulation

PNAS | 3 of 9
https://doi.org/10.1073/pnas.2015685118

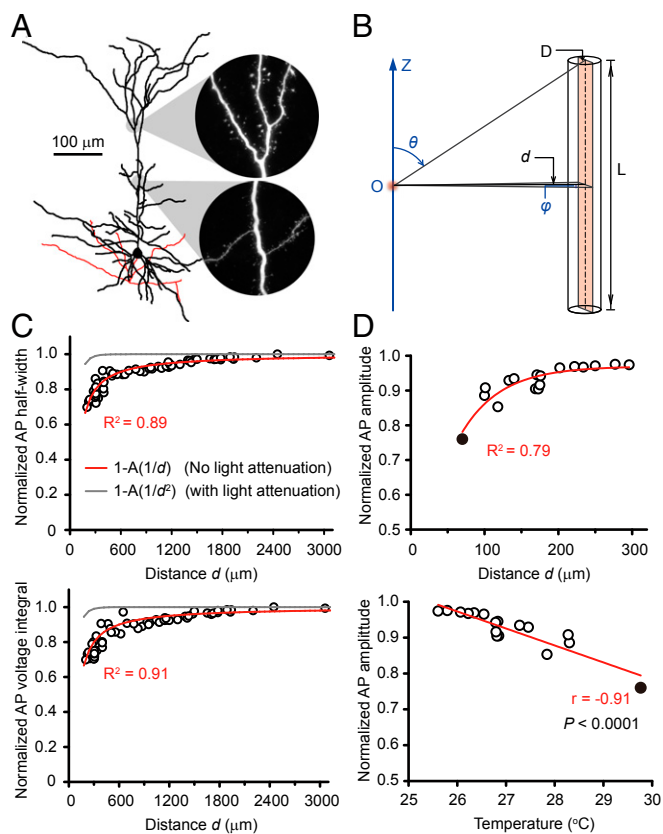**Fig. 3.** MIRS exerts long-distance nonthermal effects on AP waveforms. (*A*) A reconstructed layer-5 PC with cylinder-like neurites (total dendritic length: 6,345 μm). (*B*) A cable model for calculating the MIRS energy received by a neuron. The cylinder denotes the neuron with a length *L* and a diameter *D*. The orange rectangle indicates the projected area. The label *d* indicates the vertical distance of the source to the projected area, while θ, φ, and *O* denote the applied spherical coordinates and its origin (at the light source), respectively. (*C*) Plots of AP half-width and voltage integral as a function of the distance *d* from the MIRS fiber tip. The circles indicate the experimental data (*n* = 19 cells), as normalized to those in control. The red and gray curves denote the theoretical model (Eqs. 1 and 2 in *SI Appendix, Methods*) results. The diameter of the soma is typically 10 to 20 μm. We set the adjustable parameter *A* = 64 μm after fitting experimental data with the red curves and applied this value to generate the gray curves. (*D*) Plots of the normalized AP peak amplitudes (*n* = 20 cells) as a function of the distance *d* and temperature. The filled circles are the average data from seven cells at 70 μm. The red lines represent single exponential fit (*Top*) and linear regression fit (*Bottom*).

temperature changes. Together, these results reveal a nonthermal and long-distance effect of MIRS on AP waveforms.

MIRS Preferentially Modulates Voltage-Gated K⁺ Channels. To investigate whether MIRS-induced reduction in input resistance (Fig. 1 *E–G*) could explain the change in AP waveform and the gain control over spiking activities, we performed dynamic-clamp experiments to insert artificial leak conductances to decrease the input resistance to a similar extent as MIRS (*SI Appendix,* Fig. S7; also see *Materials and Methods*). In agreement with the shunting effect of leak conductance, we observed a progressive reduction in the frequency of repetitively spiking responses. However, distinct from MIRS, leak conductances showed no effect on AP waveform and depolarization block induced by strong current pulses (*SI Appendix,* Fig. S7). These results point to the existence of additional nonthermal mechanisms underlying the effect of MIRS.

Considering that MIRS may cause dramatic vibrations within biomolecules via nonlinear resonance, we speculated that channel proteins might respond to MIRS by conformational changes. We

first examined the effect of MIRS on voltage-gated Na⁺ channels that are critical for AP generation. In our recordings from somatic nucleated patches (Fig. 4), we stepped the command voltage from −100 mV (50 ms) to a series of 30-ms test pulses (from −60 to +10 mV) to examine the activation of Na⁺ currents (Fig. 4*A*). At 300 μm away from the light source, MIRS showed no significant effect on the peak amplitude, the half-activation voltage, and the activation curve slope (Fig. 4 *A–D*). Although there was a slight decrease in the inactivation slope, there was no significant change in the half-inactivation voltage. These results suggest a negligible effect of MIRS on Na⁺ channels.

Since voltage-gated K⁺ channels determine the repolarization and the duration of APs, we next investigated the effect of MIRS on the voltage dependence of these channels (Fig. 4 *E–H*). We stepped the command voltage from −100 mV (100 ms) to a series of test pulses (90 ms) from −40 to +70 mV. At 300 μm, we found a significant increase in the amplitude of K⁺ currents during MIRS (Fig. 4 *E* and *F*): The slope of the current–voltage characteristic (*I–V*) curve increased from 6.92 ± 0.78 to 7.52 ± 0.84 pA/mV ($t_6 = -4.43$, $P = 0.004$, paired Student's *t* test). Interestingly, MIRS shifted the activation curve toward hyperpolarizing V_m by ~10 mV ($V_{1/2}$: 17.84 ± 2.32 vs. 8.07 ± 2.89 mV, $n = 7$, $t_6 = 7.95$, $P = 0.2 \times 10^{-3}$, paired Student's *t* test; Fig. 4*G*), while the slope of the activation curve showed no significant change. Similar to AP half-width (Fig. 3*C*), MIRS also exerted a long-distance effect on K⁺ currents (*SI Appendix,* Fig. S8). These experiments revealed a nonthermal effect of MIRS on K⁺ channel activity, which would facilitate AP repolarization and thus shorten its duration. Together, the results indicate that MIRS exerts strong regulatory effects on neuronal responsiveness and AP waveforms, predominantly due to changes in the properties of voltage-gated K⁺ channels.

Resonance Vibration of −C=O at the Selectivity Filter Increases K⁺ Permeation. To explore the molecular dynamics (MD) mechanism underlying the MIRS effects, we constructed K⁺ and Na⁺ channel models with high ion selectivity (*Materials and Methods* and Fig. 5 *A–D*). These modeled channels have been found suitable for studying the permeation physics of biochannels including ion-selective ones (30–32). At an ambient temperature of 27 °C, an increase in MIRS intensity (53.53 THz; i.e., 5.6 μm in wavelength) caused a nonlinear enhancement of K⁺ permeability through K⁺ channels but not Na⁺ via Na⁺ channels (Fig. 5*E*). Next, we examined the temperature dependence of ion permeability (Fig. 5*F*). We found that as the temperature increased from 20 to 47 °C, the flows of both Na⁺ and K⁺ showed similar linear enhancements, consistent with the Einstein–Smoluchowski diffusion equation (33). Further vibration spectral analyses on the functional groups in the filters of ion-selective channels (−C=O for K⁺ channel, −COO⁻ for Na⁺ channel; Fig. 5*A*) revealed that one of the −C=O fingerprint peaks was located at 53.7 ± 0.4 THz, whereas all the fingerprint peaks of −COO⁻ were obviously distant from the frequency of added MIRS (Fig. 5*G*), well-consistent with the experimental spectral data of carbonyl and carboxyl groups in tissues of the CNS (34).

Hence, the bonds of carbonyl groups (−C=O) in K⁺ channels can resonantly absorb the energy from the added MIRS, whereas the bonds of carboxyl groups (−COO⁻) in Na⁺ channels cannot. The resonantly absorbed energy will directly drive the vibrations of carbonyl groups and enhance the efficiency of ion selectivity filters, resulting in an increase in K⁺ flow through the K⁺ channel.

MIRS Regulates Startle Responses in Zebrafish Larvae. Since MIRS can regulate ion channel activity and neuronal signaling, we next sought to examine whether MIRS could exert a modulatory effect on animal behavior. To this end, larval zebrafish (*Danio rerio*) with pan-neuronal expression of GCaMP6f was subjected
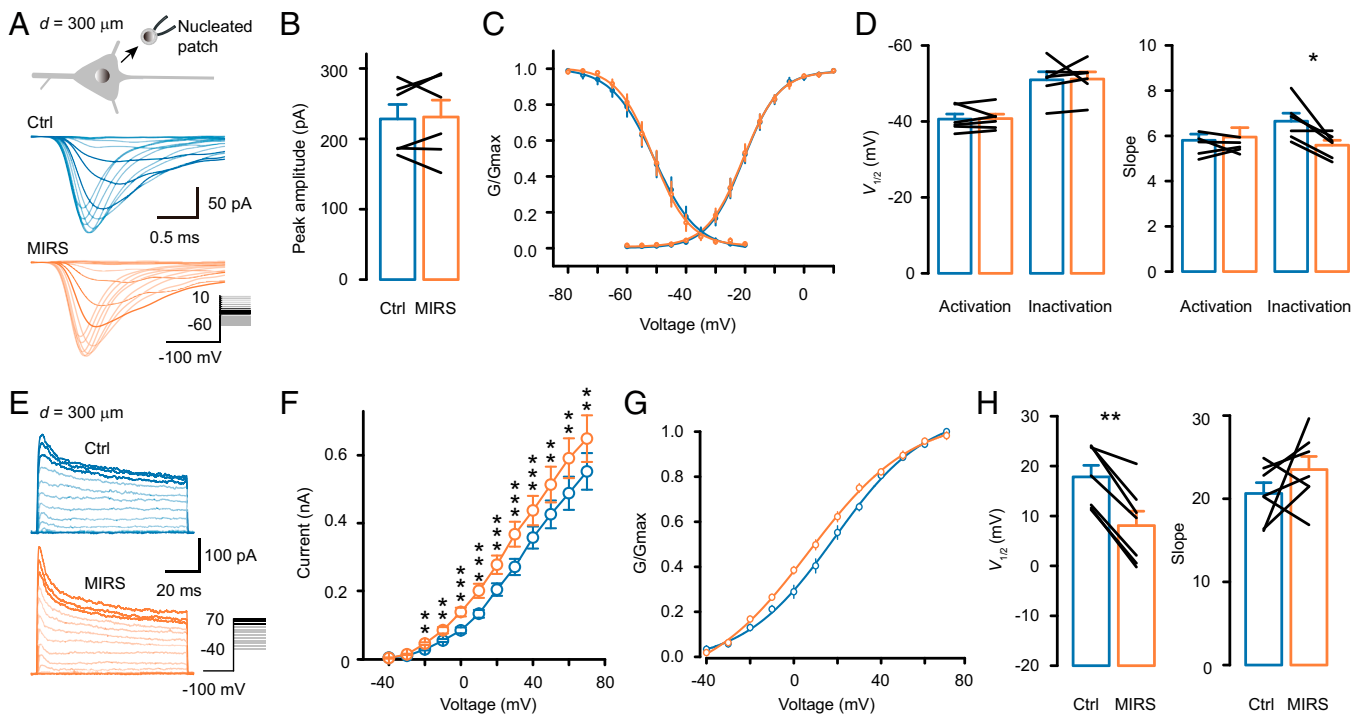
www.manaraa.com

Fig. 4. MIRS enhances K^{+} but not Na^{+} currents. (*A*–*D*) Effects of MIRS (300 μm away from the nucleated patch) on voltage-gated Na^{+} currents. (*E*–*H*) Effects of MIRS on voltage-gated K^{+} currents. (*A*) Schematic diagram of a somatic nucleated patch (*Top*) and representative families of Na^{+} currents in control (blue) and during MIRS (orange). (*A*, *Inset*) Voltage commands. (*B*) Peak amplitudes of Na^{+} currents. (*C*) Activation and steady-state inactivation curves of Na^{+} currents. (*D*) Comparison of the half-activation and -inactivation voltages and the corresponding slopes before and during MIRS. (*E*) Representative families of K^{+} currents evoked by a series of step voltages (*Inset*) in control (blue) and during MIRS (orange). (*F*) I–V curves of K^{+} currents. (*G*) Activation curves of the K^{+} currents. (*H*) Group data comparing the half-activation voltages and the slopes. *$P < 0.05$, **$P < 0.01$, and ***$P < 0.001$. Paired Student's t test. Error bars represent SEM.

to violet light stimulation (VLS) to trigger startle responses. We asked whether the behavioral responses and brain activity would be modulated when VLS was combined with MIRS. Here, the tip of a MIRS fiber was positioned 250 to 300 μm away from the zebrafish and pointed toward the fish head (*Materials and Methods* and Fig. 6*A*). The anterior body of the fish was embedded in agarose. The agarose surrounding the forebrain and the posterior body was removed and the tail was capable of swimming freely (35) (Fig. 6 *B* and *C*). The animal was mounted in a chamber perfused with E2 embryo medium to avoid the thermal effect of MIRS (*Materials and Methods*), similar to the conditions for slice recording. Whole-brain Ca^{2+} activity was monitored using light-field microscopy (36).

Consistent with previous findings (37), a brief VLS (wavelength: 405 nm; duration: 1 s) triggered a C-bend startle response in an intensity-dependent manner. With increasing VLS intensity, the maximum tail angle and the maximum angular velocity during the startle response increased progressively (Fig. 6 *D* and *E*). VLS evoked Ca^{2+} signals that reflect spiking activities in a few brain regions (Fig. 6*F*), particularly arborization field 9 (AF9) that receives axons from retinal ganglion cells responding to luminance changes (38). Consistent with the inhibitory effect on neuronal activity induced by a weak stimulus in the brain slice (Fig. 1), MIRS significantly reduced the Ca^{2+} increase at AF9 induced by low-intensity VLS (159 μW/mm^{2}; Fig. 6*G*). In response to strong VLS (851 μW/mm^{2}), however, Ca^{2+} signals at AF9 showed no significant change during MIRS. MIRS alone evoked no significant change in motor activity of the tail. In contrast, it substantially modulated the startle responses by a sharp increase in the slope of the sensorimotor input–output curve (Fig. 6 *D* and *E*). As a result, MIRS inhibited escape responses to weak but enhanced those to strong VLS. Together, our results indicate that

MIRS is able to modulate neuronal activities and sensorimotor reflexive behavior in larval zebrafish.

Discussion

In this study, we found that MIRS provides nonthermal, long-distance, and reversible modulation of neuronal signaling. It decreases neuronal responses to small inputs but increases those to larger inputs, providing a gain control over neuronal responsiveness. In addition, MIRS also shortens AP waveforms by enhancing voltage-gated K^{+} but not Na^{+} currents. MD simulation revealed that MIRS may resonantly regulate the efficiency of K^{+} channel ion selectivity filters enriched with carbonyl groups. We further demonstrate that MIRS is able to regulate startle responses in larval zebrafish. Therefore, MIRS with a specific wavelength could be a neuromodulation approach for the regulation of signal processing in neurons at molecular and cellular levels, as well as sensorimotor responses at the behavioral level.

Our results indicate that both positive and negative modulations of neuronal responsiveness occur in the same recorded neuron, depending on the strength of current stimulation or the level of ongoing firing rate (Fig. 1 and *SI Appendix*, Fig. S4). An increase in membrane conductance (i.e., decrease in input resistance) will lead to a reduction in neuronal spiking activities (39), an effect known as shunting inhibition (subtractive effect). In our experiments, the reduced neuronal responsiveness to small current pulses may largely result from the MIRS-induced decrease in cell input resistance (Fig. 1 and *SI Appendix*, Fig. S7). However, the enhanced excitability in response to larger current injections could be attributable to the shortened AP duration and the increased afterhyperpolarization resulting from increases in K^{+} currents. In addition, the increased K^{+} currents during MIRS dramatically reduced the depolarization block and thus support repetitive firing
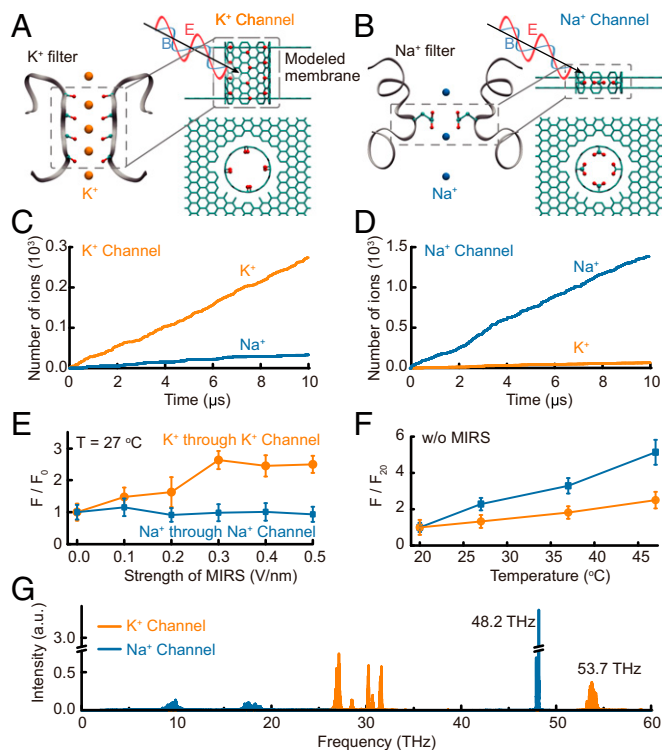
Liu et al.
Nonthermal and reversible control of neuronal signaling and behavior by midinfrared stimulation

www.manaraa.com

NEUROSCIENCE

Fig. 5. Molecular dynamics simulations reveal distinct modulation of K+ and Na+ channels by MIRS. (*A* and *B*) Modeled K+ and Na+ channels. (*A* and *B*, *Left*) Specific peptide structure of the ion selectivity filter (PDB ID codes 1K4C for the K+ filter and 3RVY for the Na+ filter). The red and cyan balls indicate the critically functional atoms oxygen and carbon of the filter on the protein chains (gray ribbons); orange and blue denote individual K+ and Na+, respectively. (*A* and *B*, *Right*) Side (*Upper*) and top (*Lower*) views of the modeled filters employed in MD simulations. The cyan tube and two sheets represent the channel and its supporting bilayered membrane, respectively. The red and cyan balls denote oxygen and carbon atoms. The black arrows together with the red and blue curves indicate the added MIRS. (*C* and *D*) Selectivity efficiencies of modeled K+ (*C*) and Na+ (*D*) channels. A typical process of ion permeation through the channel. (*E* and *F*) Effects of MIRS and temperature on ion flow through the channel. The flow is normalized to the one without MIRS (F_0; *E*) or to that at a temperature of 20 °C (F_{20}; *F*). (*G*) Vibration spectra of modeled K+ (orange) and Na+ (blue) channels. The peaks at 53.7 and 48.2 THz are contributed by the –C=O and –COO⁻ vibrations, respectively.

influx at axon terminals and thus the size of postsynaptic responses (22, 42). The presynaptic V_m-dependent analog communication (24, 26) between neurons is mediated by waveform changes of axonal APs (25, 27). We then speculated that the dramatic decrease in AP duration during MIRS would have strong impacts on synaptic transmission and thus regulate signal communication and behavioral state.

Most previous studies exploring the biological effects of INS have been conducted at near-infrared wavelengths, particularly those with high absorption by water. INS can activate peripheral nerves (2) and CNS neurons (6–9) largely due to a transient increase in local temperature (10, 11). The selection of INS parameters (e.g., wavelength, pulse width, and frequency) needs to be optimal such that the temperature increase is high enough for AP generation. The thermal effect could be explained by a capacitance mechanism where the INS-induced transient heat evokes capacitive currents and thus depolarizes the membrane potential and causes AP generation (12). Heat-activated ion channels as well as voltage-gated Na+ and Ca2+ channels have also been shown to contribute to INS-induced responses (13). Calcium imaging experiments in the cortex indicate that INS could affect intracellular calcium dynamics in both neurons and astrocytes (43). In addition to INS-induced excitation, inhibitory effects on spiking activity (44) and AP conduction (45) would also occur when appropriate laser parameters (such as laser operation mode, pulse width, and frequency) are selected, possibly resulting from the activation of voltage-gated K+ channels (46).

In this study, however, we intended to choose a wavelength with low water absorption in the midinfrared range. In our experimental conditions, MIRS still caused an increase in temperature but only near the fiber tip (<200 μm). Neurons 70 μm away from the light source exhibited V_m depolarization (*SI Appendix*, Fig. S4C); those 300 μm away, however, showed no change in the resting V_m (Fig. 1H). In addition, effects caused by similar temperature increases were significantly smaller than those of MIRS at 70 μm (Fig. 2C), suggesting that at locations near the fiber tip, MIRS exerts both thermal and nonthermal effects on neuronal signaling. Previous findings (28) together with our measurement of infrared light attenuation by ACSF (*SI Appendix*, Fig. S1) suggest a low attenuation in solution at the wavelength used in this study. The temperature increase near the fiber tip could be attributable to the superhigh power density at the point light source (the Beer–Lambert law) (47) and heat generation at the source–solution interface.

The mechanism underlying the thermal effect near the MIRS fiber tip should be similar to that of near-infrared stimulation. However, the nonthermal effect in cells distant from the fiber tip may result from nonlinear resonances between MIRS and the vibration of particular chemical bonds in neurons. The frequency of applied MIRS falls within the vibration range of carbonyl groups (16), which are enriched in proteins as well as phospholipid bilayers. It is thus expected that the resonances together with coherence would cause high-efficiency energy capture and utilization (48), resulting in an immediate conformational change in channel proteins and consequent alterations of their functions. Indeed, MIRS selectively increases K+ currents and shifts the activation curves toward hyperpolarizing potentials by ~10 mV (Fig. 4). Surprisingly, MIRS produces negligible changes in Na+ currents. Our MD simulations revealed that MIRS-induced resonance vibration of the carbonyl groups at the K+ selectivity filter increases the efficiency of the filter and thus the permeability of the channel (Fig. 5). In contrast, due to mismatch of the MIRS frequency and the carboxyl group vibration at the Na+ channel filter, no obvious change in Na+ permeability would occur. These simulation results well explain the selective effect of MIRS on the voltage-gated K+ currents, as well as the regulatory effect on input resistance that is largely governed by resting K+ channels. Together with the shunting inhibition, these effects induced by MIRS

in response to strong stimulation (Fig. 1). As a result, the slope of the input–output curve is significantly increased by MIRS, indicating a multiplicative gain control of the neuronal responsiveness. Gain modulation represents an important mechanism by which neurons integrate information from different modalities of sensory, motor, and higher-order cognition (40, 41). MIRS-induced gain modulation may provide an effective way to regulate brain functions. Indeed, MIRS reduced zebrafish startle responses induced by weak sensory stimulation but enhanced those by strong stimulation. Our data suggest that MIRS may only regulate weak (but not strong) VLS-induced Ca2+ signals at AF9, a brain region that receives retinal ganglion cell inputs and responds to luminance change (35). We speculate a more complicated mechanism underlying the enhanced startle responses to strong sensory inputs because MIRS could also regulate the neural activity in many other brain regions that contribute to sensorimotor transformation.

Traditionally, APs are considered as all-or-none digital signals with stereotypical amplitude and shape. The AP waveform, however, is actually subject to change in different physiological conditions including high-frequency firing (42) and V_m fluctuation (24). Alteration of AP waveforms would regulate the Ca2+
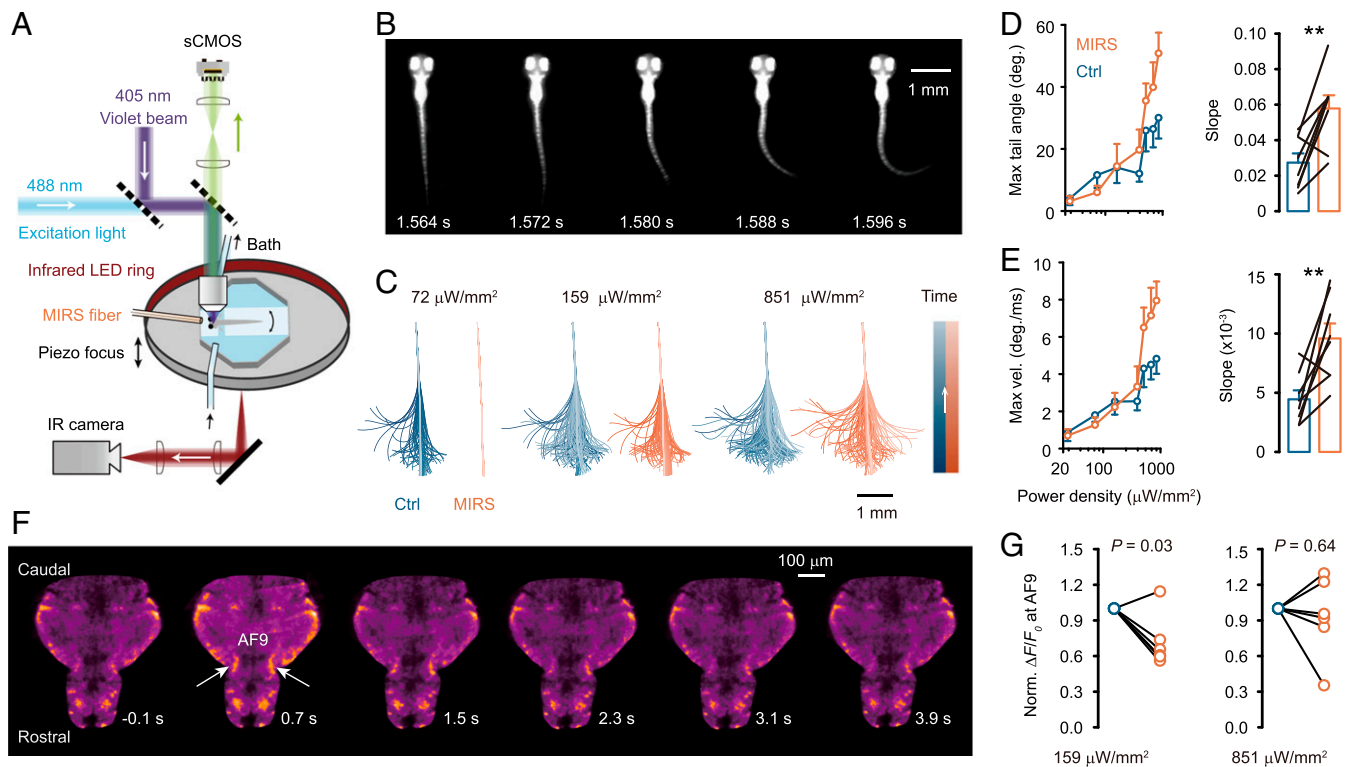
Fig. 6. MIRS regulates VLS-induced neural activity and startle responses in larval zebrafish. (*A*) Schematic drawing of the calcium (sCMOS) and behavior (infrared [IR] camera) imaging system, together with the arrangement of bath perfusion, violet light stimulation, and near-infrared illumination (LED ring). (*B*) A representative larval zebrafish showing the initial movement of a C-start response induced by VLS (duration: 1 s; onset time: 0 s). (*C*) Video-captured tail positions (presented in chronological order by gradient color) in single trials with VLS at the given power densities. Note that MIRS inhibits C-start responses to weak VSL but enhances those to high-intensity stimulation. (*D* and *E*) VLS intensity-dependent tail movement (*D*, the maximum tail angle and its slope; *E*, the maximum angular velocity and its slope) and the regulation by MIRS. (*F*) Representative single horizontal section showing fish brain Ca^{2+} signals at the given time points in a trial. (*G*) Group data showing the effect of MIRS on fluorescence signals (normalized to control) in AF9 during the time window from 0.5 to 0.9 s after the withdrawal of VLS (also see *Materials and Methods*). The intensities for weak and strong VLS are shown. **$P < 0.01$. Paired Student's *t* test. Error bars represent SEM.

synergistically modulate neuronal responsiveness and shape AP waveforms.

In agreement with the nonthermal effect of MIRS, recent simulation studies suggest that terahertz EM waves could regulate the function of biomolecules. Application of 44-THz EM waves could accelerate the unwinding process of DNA duplexes via the resonance between the wave and the vibration of bases connected via hydrogen bonds (49). An EM wave of 1.39 THz could nonthermally enhance water permeation through the water channel aquaporin, attributable to resonant absorption by the one-dimensionally confined water in the channel pore but not the bulk water outside the channel (50). Our results in this study provide experimental evidence showing a nonthermal effect of midinfrared EM waves on channel proteins and their related neural functions.

In comparison with optogenetic stimulation (1), MIRS requires no genetic manipulation and thus is more suitable for use in human subjects. Our experiments also showed that the effects of MIRS occur rapidly and reliably, and are readily reversible after withdrawal of MIRS (*SI Appendix*, Fig. S4 *D–F*). Distinct from the electrical stimulation that would activate axon fibers passing through the stimulation region, MIRS will not cause AP generation in axons, indicating a high spatial selectivity. Moreover, MIRS produces its regulatory effects on neuronal signaling across a long distance, suggesting that it does not require contact between the light source and the neural tissue, preventing tissue damage and tissue–electrode compatibility problems. The nonthermal MIRS effect may also prevent overheating of the target

tissue during stimulation. Therefore, MIRS could be used as a promising form of neuromodulation for brain function regulation and brain disease therapy.

Materials and Methods

Electrophysiological Recordings from Mouse Neocortical Slices. The use and care of mouse complied with the guidelines of the Animal Advisory Committee at the State Key Laboratory of Cognitive Neuroscience and Learning, Beijing Normal University. After preparation (*SI Appendix, Methods*), the slices were transferred into a recording chamber and perfused with ACSF (0.9 mL/min). Cortical neurons were visualized with an upright infrared differential interference contrast microscope (BX51WI; Olympus) equipped with a water-immersed objective (40×, numerical aperture 0.8). We performed current-clamp whole-cell recording from the soma of layer-5 pyramidal cells to investigate passive membrane properties, neuronal excitability, and AP waveforms before and during MIRS. In these experiments, patch pipettes were filled with a K^+-based internal solution containing 140 mM K-gluconate, 3 mM KCl, 2 mM $MgCl_2$, 10 mM Hepes, 0.2 mM ethylene glycol tetraacetic acid (EGTA), and 2 mM Na_2ATP (307 mOsm, pH 7.23 with KOH). We also added 0.2% biocytin to the solution for cell staining after the experiments. The patch pipettes had an impedance of 4 to 6 MΩ. Electrical signals were acquired using a MultiClamp 700B amplifier (Molecular Devices), digitized, and sampled by Micro 1401 mk II (Cambridge Electronic Design) at 25 kHz using spike2 software. Dynamic clamp was achieved using Power1401-3 and Signal software (Cambridge Electronic Design). A linear leak model was used to generate artificial leak conductances with a reversal potential of −60 mV. We chose to set the injected leak conductances to 1, 2, and 4 nS because they reduced the input resistance by about 12, 20, and 38%, respectively, equivalent to the MIRS-induced effect. The liquid junction potential (~15 mV) was not corrected in the text and figures.

Liu et al.
Nonthermal and reversible control of neuronal signaling and behavior by midinfrared stimulation

PNAS | 7 of 9
https://doi.org/10.1073/pnas.2015685118

To examine properties of voltage-gated Na^+ currents, we obtained nucleated patches from the soma (23). The patch pipettes were filled with a Cs^+-based internal solution containing 140 mM CsCl, 2 mM $MgCl_2$, 2 mM Na_2ATP, 10 mM Hepes, and 10 mM EGTA (287 mOsm, pH 7.2 with CsOH). We included 3 mM 4-AP and 100 μM $CdCl_2$ in the bath solution to block voltage-gated K^+ currents and Ca^{2+} currents. To isolate voltage-gated K^+ currents, we used the K^+-based pipette solution and added tetrodotoxin (1 μM) and $CdCl_2$ (100 μM) to the bath. Analysis of the electrophysiological and morphological data can be found in *SI Appendix, Methods*.

Calcium Imaging and Behavioral Test in Larval Zebrafish. The handling and care of zebrafish complied with guidelines and regulations of the Animal Resources Center at the University of Science and Technology of China (USTC). The effects of MIRS on neuronal activity and behavior were examined in larval zebrafish (huc:gcamp6f, 5 to 7 d postfertilization). The larvae were raised in E2 embryo medium (containing 7.5 mM NaCl, 0.25 mM KCl, 0.5 mM $MgSO_4$, 0.075 mM KH_2PO_4, 0.025 mM Na_2HPO_4, 0.5 mM $CaCl_2$, and 0.35 mM $NaHCO_3$; also with 0.5 mg/L methylene blue) at 28.5 °C and with a 14-h light and 10-h dark cycle. They were fed with paramecia from postfertilization day 4. For calcium and behavioral imaging, the zebrafish larvae were transferred to a chamber similar to that for brain slice recording and perfused with 10% E2 embryo medium at 0.9 mL/min. The body segment from the hindbrain to the fins was embedded and thus immobilized in 2% low–melting-point agarose, but the tail was allowed to move freely. Both eyes and the head were exposed for MIRS, and the perfusion system was able to prevent the heat accumulation and temperature increase during MIRS. These experiments were carried out at room temperature (23 to 25 °C). Similar to the application of MIRS in brain slice experiments, the distance between the MIRS fiber tip and the zebrafish head was 250 to 300 μm. To accurately place the MIRS fiber mounted on a manipulator, we first moved the fiber toward the head and almost touched the skin, and then withdrew the fiber along its axis by 250 to 300 μm.

The light-emitting diode (LED) light (M405LP1-C5; Thorlabs) was optically filtered (FBH405-10; Thorlabs) to obtain violet light at a wavelength of 405 nm (±5 nm) for violet light stimulation. This stimulation beam was then focused together with the fluorescence excitation light at 488 nm (for GCaMP6f) into a spot ~2 mm in diameter. The violet light could evoke a startle response and C-start escape behavior in the larval zebrafish. We varied the power density of the violet beam (24, 72, 159, 392, 511, 684, and 851 μW/mm^2) to examine the intensity dependence of the startle response. The behavior of the fish was monitored with a customized optical system (composed of two convex lenses and an infrared high-speed camera; Basler; acA2000-165umNIR; 0.66×) at 250 Hz. For each larva, we obtained 5 to 10 trials for each stimulus intensity. The timing of the visual stimulus was controlled by LabVIEW. The whole duration of each trial was 4.5 s. For each trial, the larva was initially allowed to rest for 0.5 s followed by 1-s VLS. Trials with swimming behavior during the initial 0.5-s time window were discarded. Control trials and MIRS trials with different VLS intensities were carried out randomly. Calcium imaging was achieved using a customized light-field microscope (36) equipped with a water-immersion objective (Nikon; N25X-APO-MP). The acquisition of light-field images (10 Hz) was conducted by Micro-Manager (1.4.22). We utilized a high-speed data acquisition card (PCIe-6321; National Instruments) as the pulse generator to synchronize calcium and behavior imaging. Procedures of data analysis are provided in *SI Appendix, Methods*.

MIRS Source. A pulsed quantum cascade laser (daylight solution; MIRcat Tunable Mid-IR) was used for MIRS stimulation. The laser emits infrared radiation between 5 and 11 μm (range of pulse width: 100 to 500 ns; pulse repetition rate: 10 to 100 kHz). The laser output was coupled to an infrared fiber (IRF-S-9; IRflex) with a core diameter of 9 μm and a cladding diameter of 170 μm (also with a thin coat of glass). The position of the fiber output end was controlled by a micromanipulator (MP-225; Sutter Instruments). MIRS with a wavelength λ of 5.6 μm was applied to the recorded cell with precisely measured distance. The duration of MIRS varied from 10 to 200 s covering the whole periods of testing for its effects. During the stimulation period, a series of midinfrared light pulses (500 ns in width for each pulse) with a repetition rate of 100 kHz was delivered to the recorded cell.

According to the Beer–Lambert law (47) and ACSF attenuation coefficient (*SI Appendix, Methods* and Fig. S1) as well as a point source model for the MIRS fiber tip, the power densities at 70 and 300 μm away from the MIRS fiber tip are estimated as 0.093 and 0.003 μW/μm^2, respectively. The local temperature changes were measured using carbon fibers (*SI Appendix, Methods*).

Molecular Dynamics Simulations. All simulations were performed using the software GROMACS 5.1.4 (51). Crystal structure data reveal that both K^+ and Na^+ channels are formed from a tetrameric arrangement of protein chains and include a narrow pore region (selectivity filter) known to dictate ion selectivity (52–54). In the process of ions permeating through the filter, they are almost completely dehydrated and the oxygen-included functional groups partially compensate for this effect in the filter region (52–55). The filter of the K^+-selective channel is lined by four rings of backbone carbonyl groups (Fig. 5 *A*, *Left*; Protein Data Bank [PDB] ID code 1K4C) (53), whereas the selectivity filter of the Na^+ channel has four anionic residues in a ring including four carboxylate groups (Fig. 5 *B*, *Left*; PDB ID code 3RVY) (54). Therefore, based on the crystal structures of K^+ and Na^+ channels, we designed two ion-selective filter models for MD simulations: one carbon nanotube with carbonyl groups for K^+ channels (Fig. 5 *A*, *Right*) (31) and with carboxylate groups for Na^+ channels (Fig. 5 *B*, *Right*) (30, 55). In these models, the nanotube simulates the structural region of the channel protein, while the added −C=O and −COO$^-$ act as the functional groups for K^+ and Na^+ selectivity, respectively. Moreover, two sheets of graphene were employed to simulate the membrane that supports the channel (the thickness of the membrane matches the filter length: 1.21 nm for the K^+ channel, and 0.24 nm for the Na^+ channel).

According to the physics of native filters, we constructed two simulation systems: a K^+-selective filter system (Fig. 5*A*) (31) and an Na^+-selective filter system (Fig. 5*B*) (30, 55). All the selective filters were located at the center of a simulation box where the dimensions are initially set as $L_X = 5.0$ nm, $L_Y = 5.2$ nm, $L_Z = 5.0$ nm for the K^+-selective filter system and $L_Z = 4.1$ nm for the Na^+-selective filter system. All the selective filters were embedded into two graphene sheets that play the role of the supporting membrane. We first filled the K^+-selective filter system with 2,800 TIP3P-modeled water molecules, 60 K^+, and 60 Cl^- to examine the permeation of K^+ through the modeled channel. After that, K^+ was replaced by Na^+ to test the permeation of Na^+ through the K^+ channel. For the Na^+-selective filter system, considering that each carboxylate group (−COO$^-$) in the filter carries a net charge of −1 e, we filled the Na^+-selective filter system with 2,800 water molecules, 60 Na^+, and 56 Cl^- to make the system electro-neutral. Replacing Na^+ by K^+, we further obtained another simulation system for testing the permeation of K^+. *SI Appendix, Methods* has additional information about the simulations.

Statistical Analysis. All computation was performed using Spike 2 and MATLAB (MathWorks). The sample size was not predetermined. We determined the sample size based on numbers previously reported. All measurements were taken from distinct samples. To compare between conditions (control vs. MIRS), we obtained data from at least six cells from different animals. No samples were excluded from the analysis. The data are presented as mean ± SEM. Error bars in the figures also represent SEM. Unless otherwise specified, two-tailed paired Student's t test was used if the data were paired. For two independent observations, nonnormal data were compared using an independent Wilcoxon rank-sum test. For more than two independent observations, repeated-measures ANOVA with post hoc Bonferroni's multiple comparison was applied. Differences were considered to be significant if $P < 0.05$.

Data Availability. All study data are included in the article and/or *SI Appendix*.

1. K. Deisseroth, Optogenetics: 10 years of microbial opsins in neuroscience. *Nat. Neurosci.* **18**, 1213–1225 (2015).
2. J. Wells, P. Konrad, C. Kao, E. D. Jansen, A. Mahadevan-Jansen, Pulsed laser versus electrical energy for peripheral nerve stimulation. *J. Neurosci. Methods* **163**, 326–337 (2007).
3. A. D. Izzo, C. P. Richter, E. D. Jansen, J. T. Walsh, Jr, Laser stimulation of the auditory nerve. *Lasers Surg. Med.* **38**, 745–753 (2006).
4. S. M. Rajguru *et al.*, Infrared photostimulation of the crista ampullaris. *J. Physiol.* **589**, 1283–1294 (2011).
5. M. W. Jenkins *et al.*, Optical pacing of the embryonic heart. *Nat. Photonics* **4**, 623–626 (2010).
6. J. M. Cayce *et al.*, Infrared neural stimulation of thalamocortical brain slices. *IEEE J. Sel. Top. Quantum Electron.* **16**, 565–572 (2010).
7. J. M. Cayce, R. M. Friedman, E. D. Jansen, A. Mahavaden-Jansen, A. W. Roe, Pulsed infrared light alters neural activity in rat somatosensory cortex in vivo. *Neuroimage* **57**, 155–166 (2011).
8. J. M. Cayce *et al.*, Infrared neural stimulation of primary visual cortex in non-human primates. *Neuroimage* **84**, 181–190 (2014).

8 of 9 | PNAS
https://doi.org/10.1073/pnas.2015685118

Liu et al.
Nonthermal and reversible control of neuronal signaling and behavior by midinfrared

9. A. G. Xu *et al*., Focal infrared neural stimulation with high-field functional MRI: A rapid way to map mesoscale brain connectomes. *Sci. Adv.* **5**, eaau7046 (2019).

10. J. Wells *et al*., Optical stimulation of neural tissue in vivo. *Opt. Lett.* **30**, 504–506 (2005).

11. M. Chernov, A. W. Roe, Infrared neural stimulation: A new stimulation tool for central nervous system applications. *Neurophotonics* **1**, 011011 (2014).

12. M. G. Shapiro, K. Homma, S. Villarreal, C.-P. Richter, F. Bezanilla, Infrared light excites cells by changing their electrical capacitance. *Nat. Commun.* **3**, 736 (2012).

13. E. S. Albert *et al*., TRPV4 channels mediate the infrared laser-evoked response in sensory neurons. *J. Neurophysiol.* **107**, 3227–3234 (2012).

14. M. M. Chernov, G. Chen, A. W. Roe, Histological assessment of thermal damage in the brain following infrared neural stimulation. *Brain Stimul.* **7**, 476–482 (2014).

15. B. M. Fischer, M. Walther, P. Uhd Jepsen, Far-infrared vibrational modes of DNA components studied by terahertz time-domain spectroscopy. *Phys. Med. Biol.* **47**, 3807–3814 (2002).

16. Z. Movasaghi, S. Rehman, I. Rehman, Fourier transform infrared (FTIR) spectroscopy of biological tissues. *Appl. Spectrosc. Rev.* **43**, 134–179 (2008).

17. A. Matei, N. Drichko, B. Gompf, M. Dressel, Far-infrared spectra of amino acids. *Chem. Phys.* **316**, 61–71 (2005).

18. H. Fröhlich, The extraordinary dielectric properties of biological materials and the action of enzymes. *Proc. Natl. Acad. Sci. U.S.A.* **72**, 4211–4215 (1975).

19. Y. Feng, R. D. Beger, X. Hua, E. W. Prohofsky, Breathing modes near a junction of DNA double helices. *Phys. Rev. A Gen. Phys.* **40**, 4612–4619 (1989).

20. M. Blank, R. Goodman, Do electromagnetic fields interact directly with DNA? *Bioelectromagnetics* **18**, 111–115 (1997).

21. O. P. Cherkasova, V. I. Fedorov, E. F. Nemova, A. S. Pogodin, Influence of terahertz laser radiation on the spectral characteristics and functional properties of albumin. *Opt. Spectrosc.* **107**, 534–537 (2009).

22. D. Debanne, E. Campanac, A. Bialowas, E. Carlier, G. Alcaraz, Axon physiology. *Physiol. Rev.* **91**, 555–602 (2011).

23. W. Hu *et al*., Distinct contributions of Na(v)1.6 and Na(v)1.2 in action potential initiation and backpropagation. *Nat. Neurosci.* **12**, 996–1002 (2009).

24. Y. Shu, A. Hasenstaub, A. Duque, Y. Yu, D. A. McCormick, Modulation of intracortical synaptic potentials by presynaptic somatic membrane potential. *Nature* **441**, 761–765 (2006).

25. Y. Shu, Y. Yu, J. Yang, D. A. McCormick, Selective control of cortical axonal spikes by a slowly inactivating K$^+$ current. *Proc. Natl. Acad. Sci. U.S.A.* **104**, 11453–11458 (2007).

26. H. Alle, J. R. Geiger, Combined analog and action potential coding in hippocampal mossy fibers. *Science* **311**, 1290–1293 (2006).

27. M. H. Kole, J. J. Letzkus, G. J. Stuart, Axon initial segment Kv1 channels control axonal action potential waveform and synaptic efficacy. *Neuron* **55**, 633–647 (2007).

28. Y. Maréchal, The molecular structure of liquid water delivered by absorption spectroscopy in the whole IR region completed with thermodynamics data. *J. Mol. Struct.* **1004**, 146–155 (2011).

29. J. Yao, B. Liu, F. Qin, Rapid temperature jump by infrared diode laser irradiation for patch-clamp studies. *Biophys. J.* **96**, 3611–3619 (2009).

30. R. García-Fandiño, M. S. Sansom, Designing biomimetic pores based on carbon nanotubes. *Proc. Natl. Acad. Sci. U.S.A.* **109**, 6939–6944 (2012).

31. X. Gong, J. Li, K. Xu, J. Wang, H. Yang, A controllable molecular sieve for Na$^+$ and K$^+$ ions. *J. Am. Chem. Soc.* **132**, 1873–1877 (2010).

32. R. H. Tunuguntla *et al*., Enhanced water permeability and tunable ion selectivity in subnanometer carbon nanotube porins. *Science* **357**, 792–796 (2017).

33. K. A. Dill, S. Bromberg, *Molecular Driving Forces: Statistical Thermodynamics in Biology, Chemistry, Physics, and Nanoscience* (Garland Science, New York, 2012).

34. S. Caine, P. Heraud, M. J. Tobin, D. McNaughton, C. C. Bernard, The application of Fourier transform infrared microspectroscopy for the study of diseased central nervous system tissue. *Neuroimage* **59**, 3624–3640 (2012).

35. I. Temizer, J. C. Donovan, H. Baier, J. L. Semmelhack, A visual pathway for looming-evoked escape in larval zebrafish. *Curr. Biol.* **25**, 1823–1834 (2015).

36. L. Cong *et al*., Rapid whole brain imaging of neural activity in freely behaving larval zebrafish (*Danio rerio*). *eLife* **6**, e28158 (2017).

37. G. Bruni *et al*., Zebrafish behavioral profiling identifies multitarget antipsychotic-like compounds. *Nat. Chem. Biol.* **12**, 559–566 (2016).

38. E. Robles, E. Laurell, H. Baier, The retinal projectome reveals brain-area-specific visual representations generated by ganglion cell diversity. *Curr. Biol.* **24**, 2085–2096 (2014).

39. G. R. Holt, C. Koch, Shunting inhibition does not have a divisive effect on firing rates. *Neural Comput.* **9**, 1001–1013 (1997).

40. F. S. Chance, L. F. Abbott, A. D. Reyes, Gain modulation from background synaptic input. *Neuron* **35**, 773–782 (2002).

41. E. Salinas, P. Thier, Gain modulation: A major computational principle of the central nervous system. *Neuron* **27**, 15–21 (2000).

42. J. R. Geiger, P. Jonas, Dynamic control of presynaptic Ca(2+) inflow by fast-inactivating K(+) channels in hippocampal mossy fiber boutons. *Neuron* **28**, 927–939 (2000).

43. J. M. Cayce *et al*., Calcium imaging of infrared-stimulated activity in rodent brain. *Cell Calcium* **55**, 183–190 (2014).

44. Q. Xia, T. Nyberg, Inhibition of cortical neural networks using infrared laser. *J. Biophotonics* **12**, e201800403 (2019).

45. A. R. Duke *et al*., Transient and selective suppression of neural activity with infrared light. *Sci. Rep.* **3**, 2600 (2013).

46. M. Ganguly *et al*., Voltage-gated potassium channels are critical for infrared inhibition of action potentials: An experimental study. *Neurophotonics* **6**, 040501 (2019).

47. T. G. Mayerhöfer, H. Mutschke, J. Popp, Employing theories far beyond their limits—The case of the (Boguer-) Beer–Lambert law. *ChemPhysChem* **17**, 1948–1955 (2016).

48. B. Song, Y. Shu, Cell vibron polariton resonantly self-confined in the myelin sheath of nerve. *Nano Res.* **13**, 38–44 (2019).

49. K. Wu *et al*., Terahertz wave accelerates DNA unwinding: A molecular dynamics simulation study. *J. Phys. Chem. Lett.* **11**, 7002–7008 (2020).

50. Z. Zhu, C. Chang, Y. Shu, B. Song, Transition to a superpermeation phase of confined water induced by a terahertz electromagnetic wave. *J. Phys. Chem. Lett.* **11**, 256–262 (2020).

51. M. Abraham *et al*., GROMACS: High performance molecular simulations through multi-level parallelism from laptops to supercomputers. *SoftwareX* **1**, 19–25 (2013).

52. D. A. Doyle *et al*., The structure of the potassium channel: Molecular basis of K$^+$ conduction and selectivity. *Science* **280**, 69–77 (1998).

53. S. Y. Noskov, S. Bernèche, B. Roux, Control of ion selectivity in potassium channels by electrostatic and dynamic properties of carbonyl ligands. *Nature* **431**, 830–834 (2004).

54. J. Payandeh, T. Scheuer, N. Zheng, W. A. Catterall, The crystal structure of a voltage-gated sodium channel. *Nature* **475**, 353–358 (2011).

55. Z. He, J. Zhou, X. Lu, B. Corry, Bioinspired graphene nanopores with voltage-tunable ion selectivity for Na(+) and K(+). *ACS Nano* **7**, 10148–10157 (2013).